Efficient magnetic-field amplification due to the Kelvin-Helmholtz instability in binary neutron star mergers

Kenta Kiuchi,[1] Pablo Cerdá-Durán,[2] Koutarou Kyutoku,[3] Yuichiro Sekiguchi,[4] and Masaru Shibata[5]

[1] *Yukawa Institute for Theoretical Physics, Kyoto University, Kyoto, 606-8502, Japan*
[2] *Departamento de Astronomía y Astrofísica, Universitat de Valéncia, 46100 Burjassot (Valencia), Spain*
[3] *Interdisciplinary Theoretical Science (iTHES) Research Group, RIKEN, Wako, Saitama 351-0198, Japan*
[4] *Department of Physics, Toho University, Funabashi, Chiba 274-8510, Japan*
[5] *Yukawa Institute for Theoretical Physics, Kyoto University, Kyoto, 606-8502, Japan*

(Dated: November 17, 2015)

We explore magnetic-field amplification due to the Kelvin-Helmholtz instability during binary neutron star mergers. By performing high-resolution general relativistic magnetohydrodynamics simulations with a resolution of 17.5 m for 4–5 ms after the onset of the merger on the Japanese supercomputer "K", we find that an initial magnetic field of moderate maximum strength 10^{13} G is amplified at least by a factor of $\approx 10^3$. We also explore the saturation of the magnetic-field energy and our result shows that it is likely to be $\gtrsim 4\times10^{50}$ erg, which is $\gtrsim 0.1\%$ of the bulk kinetic energy of the merging binary neutron stars.

PACS numbers: 04.25.D-, 04.30.-w, 04.40.Dg

arXiv:1509.09205v2 [astro-ph.HE] 13 Nov 2015

I. INTRODUCTION.

The merger of binary neutron stars (BNS) is one of the most promising sources for the ground-based gravitational wave detectors such as advanced LIGO, advanced VIRGO, and KAGRA [1–3]. If gravitational waves from them are detected, we will be able to assess the validity of general relativity in a strong gravitational field and explore the equation of state (EOS) of neutron star (NS) matter. Furthermore, the merger of BNSs could be a central engine of short-hard gamma-ray bursts (sGRB) and the simultaneous detection of gravitational waves and sGRB will give a constraint on this merger hypothesis [4].

During the merger, the elements heavier than the iron peak elements could be synthesized via the so-called r-process [5] and it could reproduce the solar abundance pattern of the r-process heavy elements [6, 7]. The radioactively powered emission from these elements could be a strong electromagnetic transient [8–10]. Motivated by these facts, building a physically reliable model of BNS mergers is in rapid progress.

In this paper, we focus on exploring the role of the magnetic field because it is one of the universal features of NSs. The observations of binary pulsars indicate that the surface dipole magnetic-field strength is in the range of $10^{9.7-12.2}$ G [11]. Rasio and Shapiro have pointed first that the Kelvin-Helmholtz (KH) instability could significantly amplify the magnetic-field strength at the merger [12]. Price and Rosswog suggested for the first time that this could be indeed the case [13]. This instability develops in a shear layer which appears when the two stars come into contact.

It has been controversial whether this mechanism works in practice and several preliminary simulations have been reported [13–19]. The issue is that, because the growth rate of the KH instability is proportional to the wave number of the mode, high-resolution simulations together with a careful convergence study is necessary to explore this instability. Recently, the authors of Ref. [20] have performed general relativistic magnetohydrodynamics (GRMHD) simulation of the BNS merger with significantly higher resolution (by a factor ~ 2.5) than any previous simulation. They revealed that, only for a sufficiently high numerical resolution, the KH instability activates as an amplifier of the magnetic field at the merger.

However, it is still an open question to what extent the magnetic field is amplified during the merger under realistic conditions because an initial magnetic-field strength employed in Ref. [20] was assumed to be of magnetar class, i.e., $10^{14.5-16}$ G. Because the magnetic-field amplification was saturated at the maximum field strength of $\sim 10^{17}$ G, the previous simulations followed this amplification process by a factor of 10. Several local box simulations have suggested that the magnetic-field energy may be amplified by several orders of magnitude until reaching an equipartition level even if we assume moderate initial magnetic-field strength [21, 22]. In this paper, we go a step further to thoroughly explore the amplification of the magnetic field by the KH instability. Initially setting moderately strong realistic magnetic fields of maximum strength 10^{13} G, we perform GRMHD simulations of BNS mergers on the Japanese supercomputer "K" increasing the resolution by a factor 4 with respect to previous simulations by Ref. [20].

This paper is organized as follows. In Sec. II, we briefly mention the method, the grid setup, and the initial models of the BNSs. We also describe how we increase the grid resolution in the shear layer during the merger. Sections III and IV are devoted to presenting numerical results. Section V is for the discussion and the summary is given in Sec. VI.

II. METHOD, GRID SETUP, AND INITIAL MODELS.

The code is the same as that in Refs. [20, 23]; Einstein's equation is formulated based on a Baumragte-Shapiro-Shibata-Nakamura-puncture formulation [24–27] and solved by fourth-order finite differencing. GRMHD is formulated in a conservative form and solved by a high resolution shock capturing scheme together with a third-order cell reconstruction [28]. We implement a fixed mesh refinement algorithm to cover a wide dynamical range of BNS mergers. Specifically, a refinement domain labeled by l is a cuboid box of $x_{(l)} \in [-N\Delta x_{(l)}, N\Delta x_{(l)}]$, $y_{(l)} \in [-N\Delta y_{(l)}, N\Delta y_{(l)}]$, and $z_{(l)} \in [0, N\Delta z_{(l)}]$ where we assume an orbital plane symmetry. Given a grid resolution, a constant integer N specifies the size of the refinement domain. In our algorithm, N is identical for all the refinement levels. $\Delta x_{(l)}, \Delta y_{(l)}$, and $\Delta z_{(l)}$ are a grid resolution in the refinement domain l and we assume $\Delta x_{(l)} = \Delta y_{(l)} = \Delta z_{(l)}$. The grid resolution in a coarser refinement domain $l-1$ is $\Delta x_{(l-1)} = 2\Delta x_{(l)}$ with $l = 2, 3, \cdots$, and $l_{\rm max}$. $l_{\rm max}$ is the number of the refinement levels. The divergence free condition as well as the flux conservation of the magnetic field in a refinement boundary are preserved by the Balsara's algorithm [29].

To improve the grid resolution for a shear layer which appears when the two stars come into contact, we add new refinement domains at about 1 ms before the merger. The size of the new finest refinement domain is determined by the initial grid configuration; typically, the *initial* finest domain is a cuboid of $\approx (72000\ {\rm m})^3/2$. If we add one refinement domain, the *final* finest domain is a cuboid of $\approx (36000\ {\rm m})^3/2$. If we add two domains, the final finest domain is that of $\approx (18000\ {\rm m})^3/2$ (see Fig. 1 for a schematic picture). Previous simulations have suggested that the shear layer appears in a central region of radius ~ 10000 m [20]. Therefore, we increase the number of the refinement domains up to two. Table I shows the grid setup. We achieve 17.5 m resolution which is much finer than the highest-resolution in our previous simulation [20].

As a fiducial model, we choose an equal-mass irrotational binary of total mass $2.8M_\odot$. As an EOS to model the NS, we assume the H4 EOS [33]. The initial orbital angular frequency is $Gm_0\Omega/c^3 = 0.0221$ where G is the gravitational constant, m_0 is the sum of the gravitational mass in isolation, and c is the speed of light. At about 1 ms before the onset of the merger, we add a seed magnetic field whose configuration is given by

$$A_i = (-(y-y_{\rm NS})\delta^x_i + (x-x_{\rm NS})\delta^y_i)\, A_{\rm b} \times \max(P - P(0.04\rho_{\rm max}), 0)^2, \quad (2.1)$$

where $i = x, y$, and z, P is the pressure, and $\rho_{\rm max}$ is the maximum rest-mass density. $x_{\rm NS}$ and $y_{\rm NS}$ denote the coordinate center of the NS. $A_{\rm b}$ determines the maximum magnetic-field strength, which is realized at the stellar center. The observations of binary pulsars suggest that the *surface dipole* magnetic-field strength is in the range $\sim 10^{9.7} - 10^{12.2}$ G [11]. However, the interior magnetic field strength is mostly unconstrained since currents at the surface could be shielding a much stronger or weaker field in the interior. If shielding is not invoked, theoretical models of magnetized neutron star equilibria result in a typical interior magnetic field 2–5 times as large as its surface value [30–32]. We thus set the initial maximum magnetic-field strength to be 10^{13} G, which is approximately compatible with the upper observational limit mentioned above and a reasonable choice to mimic the realistic magnetic-field strength of the BNSs. To explore the saturation of the magnetic-field energy amplified by the KH instability, we artificially increase the initial magnetic-field strength up to 10^{15} G in some of our simulations.

Note that, up to 1 ms before the onset of the merger, the simulations are essentially the same as those in Ref. [20] because the magnetic field does not affect the inspiral dynamics. Table II summarizes the models with respect to the initial magnetic-field strength. During the evolution, we use a piece-wise polytrope prescription to model the H4 EOS [34] with a thermal part consisting of a gamma-law EOS with the thermal index of 1.8.

TABLE I. Grid setup for all the run. $l^0_{\rm max}(l_{\rm max})$: The number of the refinement levels of the initial (final) grid configuration. $\Delta x_{(l^0_{\rm max})}(\Delta x_{(l_{\rm max})})$: The grid spacing of the finest refinement level of the initial (final) grid configuration. N: The grid number in one positive direction.

$l^0_{\rm max}$	$l_{\rm max}$	$\Delta x_{(l^0_{\rm max})}$ [m]	$\Delta x_{(l_{\rm max})}$ [m]	N
7	7	70	70	514
7	8	70	35	514
7	9	70	17.5	514
7	7	110	110	322
7	8	110	55	322
7	9	110	27.5	322
7	7	150	150	242
7	8	150	75	242
7	9	150	37.5	242

TABLE II. The initial maximum magnetic-field strength of the BNS.

Model	$\log_{10}(B_{\rm max}$ [G])
B13	13
B14	14
B15	15

III. DYNAMICS, MAGNETIC-FIELD AMPLIFICATION, AND RESOLUTION STUDY

In this section, we describe the dynamics, magnetic-field amplification, and resolution study for the B13 run.

A. Kelvin-Helmholtz vortex formation

Figure 2 plots the rest-mass density profiles with the velocity field (the 1st row) and the vorticity profiles (the 2nd row) on the orbital plane for the $\Delta x_{(l_{\rm max})} = 17.5$ m run. The vorticity is defined as the spatial components of the following 2-form

$$\omega_{\mu\nu} = \nabla_\mu (h u_\nu) - \nabla_\nu (h u_\mu), \tag{3.1}$$

where h, u_μ, and ∇_μ are the specific enthalpy, the four velocity, and the covariant derivative with respect to the spacetime metric, respectively. We define the merger time $t_{\rm mrg}$ to be the time at which the gravitational-wave amplitude becomes maximum.

Just before the merger, a shear layer appears at the contact interface between the two stars as shown in Fig. 2(a1) (see also Fig. 5 and visualization [35]). This contact interface is subject to the KH instability. At the merger, the KH instability develops and subsequently vortices are formed in the shear layer [Figs. 2(a2) and (b2)]. Figures 2(c1)–(c4) plot the thermal component of the specific internal energy $\epsilon_{\rm th}$. A hot region appears in the shear layer. This is due to the numerical dissipation of the votrices at the finest resolution size (see also Figs. 3 and 4(c1)–(c4) and discussion in Sec. IIIC). The shock wave generated by the collision of the two stars also dissipates the vortices. Note that the KH vortices are not completely dissipated and they cascade into smaller-scale turbulence-like motion.

Subsequently, a hypermassive neutron star (HMNS) is formed. In its early phase, two dense cores are transiently formed and they collide several times [Fig. 2(a3)]. Because of their mutual interaction, the shear layer continuously appears between the two cores and additional KH vortices are successively generated [Fig. 2(b3)]. The two cores eventually merge to a single core and the shear layer disappears due to the shock heating driven by stellar oscillations, leaving behind a highly turbulence-like flow, which decays in a dissipative timescale [Figs. 2(a4), (b4), and (c4)].

We can interpret these results in the light of the KH linear stability analysis [36]. The growth rate of the KH instability is proportional to the wavenumber of the unstable mode. For a shear flow with thickness D, there is a cut-off wavenumber, $k_{\rm cutoff} \sim 2\pi/D$ above which modes do not grow [36]. In practice, this means that the fastest growing KH mode has a wavenumber, $k_{\rm KH}$ close to the cut-off and its growth rate is $\sigma_{\rm KH} \sim v_{\rm flow} k_{\rm KH}$. The right panel of Fig. 5 plots the profile of the x component of the velocity along the y axis with $x = 0$ km at $t - t_{\rm mrg} = -0.90$ ms. This figure clearly shows that D decreases with increasing the grid resolution. Therefore, $k_{\rm cutoff}$ increases as a function of $1/\Delta x_{(l_{\rm max})}$. We found that for $\Delta x_{(l_{\rm max})} = 17.5$ m run $D \approx 130$ m and $v_{\rm flow} \approx 0.1c$. With these values, the growth timescale is $\sigma_{\rm KH}^{-1} \approx 6 \times 10^{-3}$ ms which is much shorter than the dynamical timescale of ~ 0.1 ms. In reality, the scale of the shear layer should depend on other factors such as the pressure scale height at the surface of the NS and the tidal deformation. Therefore, it is not trivial that D goes to zero in the continuum limit. Nonetheless, the shear layer should be sufficiently thin and consequently the growth rate of the KH instability should be so large that the small-scale turbulence-like motion develops within the dynamical timescale.

B. Magnetic-field amplification

Due to the KH instability, turbulence-like motion is generated and this indicates that a part of the bulk kinetic energy is converted into the energy of turbulence-like motion [see also Figs. 2(b1)–(b4)]. In the presence of magnetic fields, a part of this energy is transferred to the magnetic-field energy, which results in an efficient amplification of the magnetic field. Figures 2(d1)–(d4) show the magnetic-field strength profiles on the orbital plane. A strong magnetic field of $\sim 10^{14}$ G is rapidly generated at the contact interface [Fig. 2(d2)] and it is amplified in the shear layer between the two cores [Fig. 2(d3)]. At the end of the simulation, a strongly magnetized core is formed [Fig. 2(d4)], with rms field values of $\sim 10^{15.5}$ G and peak values of $\sim 10^{17}$ G.

During this *kinematic phase*, the magnetic field is still weak and does not influence the dynamics; the magnetic field is being stretched by the overturning turbulence-like motion, which results in an exponential growth. This kinematic phase should end up with any of the following mechanisms. First, once the amplitude of the magnetic field reaches an equipartition level, the magnetic field starts playing a dynamical effect. Second, the turbulence-like motion decays within the diffusion timescale which is limited by the numerical resolution used. Third, it is the ability of the global flow to regenerate the shear flow and produce additional large-scale eddies, as described in the previous section. These limitations are discussed in subsequent sections.

C. Resolution study

Figures 3 and 4 plot the profiles of the rest-mass density, the vorticity, the thermal component of the specific internal energy, and the magnetic-field strength on the orbital plane for $\Delta x_{(l_{\rm max})} = 37.5$ and 150 m runs, respectively. For $\Delta x_{(l_{\rm max})} = 37.5$ m run, the qualitative features agree with those discussed in the previous subsections, but the formation of vortices and the magnetic-

field amplification are likely to be less prominent than those for $\Delta x_{(l_{\rm max})} = 17.5$ m run. [compare Figs. 2(b2)–(b4) and (d2)–(d4) with Figs. 3(b2)–(b4) and (d2)–(d4)]. The difference is clearer in Fig. 4 with $\Delta x_{(l_{\rm max})} = 150$ m. The scale of the vortices is smaller and the magnetic-field is amplified more efficiently in the higher-resolution run. This feature is consistent with the linear perturbation analysis of the KH instability; the growth rate of the fastest growing mode is inversely proportional to the minimum grid spacing and hence high-resolutions exhibit faster development of vortices.

The peak value of $\epsilon_{\rm th}$ in the shear layer decreases with increasing the resolution [see Figs. 2(c2)–(c3), 3(c2)–(c3), and 4(c2)–(c3)]. As discussed below, the cascade of the turbulence-like motion converts the kinetic energy to the thermal energy at the dissipation scale determined by the grid resolution. This finding is consistent with such a dissipation mechanism.

We calculate the power spectrum of the turbulence-like motion as

$$P_M(t,k) = \frac{1}{2V}\int_V \delta\tilde{\mathbf{v}}_\rho(t,\mathbf{k})\cdot\delta\tilde{\mathbf{v}}^*_\rho(t,\mathbf{k})d\Omega_k, \qquad (3.2)$$

where

$$\delta\tilde{\mathbf{v}}_\rho(t,\mathbf{k}) = \int_V e^{-i\mathbf{k}\cdot\mathbf{r}}\sqrt{\rho(t,\mathbf{x})}\delta\mathbf{v}(t,\mathbf{x})d^3r. \qquad (3.3)$$

The bold symbol denotes a spatial three vector. $\mathbf{k}$ is a wavenumber vector and $k = |\mathbf{k}|$. $d\Omega_k$ is a phase-space volume element in a spherical shell between k and $k+dk$, and V is a cuboid region of x, y[km] $\in [-4.5, 4, 5]$, z[km] $\in [0.0, 4.5]$. We choose $\mathbf{r}$ to be a position vector from the coordinate center. The velocity fluctuation $\delta\mathbf{v}(t,\mathbf{x})$ is $\mathbf{v}(t,\mathbf{x}) - \langle\mathbf{v}\rangle(\mathbf{x})$ where $\langle\cdot\rangle$ denotes the time average for the duration 0.0 ms $\leq t - t_{\rm mrg} \leq$ 2.0 ms. We evaluate $\delta\mathbf{v}$ at $t - t_{\rm mrg} = 2.0$ ms. With this, $\int P_M(t,k)dk$ corresponds to the kinetic energy density of the turbulence-like flow. Figure 6 plots the power spectrum of $\Delta x_{(l_{\rm max})} = 37.5$, 75, and 150 m runs, respectively. The amplitude at large scale in the lower-resolution run is higher than that in the higher-resolution run and the spectrum extends to a higher wavenumber in the higher-resolution run. This indicates that the energy of large-scale turbulence-like motion cascades to that of small-scale motion. The figure also indicates that there is a kinetic energy sink at the end of the turbulence cascade due to the numerical dissipation. The power excess at the highest k is the so-called *bottleneck* effect [42] and is observed always in 3D simulations of turbulence (see, e.g., [43–45]). Because energy budget of the KH instability should be the bulk kinetic energy, all the findings show that a part of the bulk kinetic energy is converted into the kinetic energy of the turbulence-like motion and subsequently thermalized at the dissipation scale.

Figure 7 plots the power spectrum of the magnetic-field energy:

$$P_B(t,k) = \frac{1}{8\pi V}\int_V \tilde{b}(t,\mathbf{k})\tilde{b}^*(t,\mathbf{k})d\Omega_k, \qquad (3.4)$$

where

$$\tilde{b}(t,\mathbf{k}) = \int_V e^{-i\mathbf{k}\cdot\mathbf{r}}b(t,\mathbf{x})d^3r. \qquad (3.5)$$

$b = \sqrt{b^\mu b_\mu}$ and b^μ is a magnetic field measured in a fluid rest frame. We evaluate b for $\Delta x_{(l_{\rm max})} = 17.5$, 27.5, 37.5, 75, and 150 m at $t - t_{\rm mrg} = 2.0$ ms as shown in the left panel of Fig. 7, respectively. As expected, the amplitude is higher in the higher-resolution run. This indicates that the kinetic energy of the turbulence-like motion is converted to the magnetic-field energy more efficiently in the higher-resolution runs.

The right panel is for $\Delta x_{(l_{\rm max})} = 17.5$ m run at $t - t_{\rm mrg} = 1.0, 2.0$ and 4.4 ms, respectively. The spectrum is relatively flat in the inertial range of the turbulent cascade and its amplitude increases with time. These features resemble the behavior of the spectrum in local simulations of a large-scale dynamos during the kinematic amplification phase (see, e.g., Fig. 2 in Ref. [46]).

In local simulations, the kinematic phase ends when the magnetic-field strength reaches an equipartition level and a slow saturation phase occurs in which large-scale field is generated (see discussion in Ref. [47]). Checking whether a large-scale dynamo is active in our simulations would require longer simulations of the saturated state. However, it is unclear if this will be indeed the case; the shear layer is pumping kinetic energy at sub km-size scales in the first few ms after the merger, feeding the turbulent cascade and making it viable dynamo action; however this initial phase eventually ends as the two cores merge and turbulence-like motion will decay in diffusive timescales, in which the dynamo may not be active anymore. We do not see any sign of a 3/2 Kazantzev spectrum during the kinematic phase, typical of small-scale dynamos, as predicted by Ref. [22].

The fact that the magnetic field power is growing at all scales indicates that the kinetic energy of the turbulence-like motion is converted into the magnetic-field energy. We estimate the kinetic energy density and the magnetic-field energy density for the highest-resolution run at $t - t_{\rm mrg} = 4.4$ ms

$$\epsilon_K = \int P_M(t,k)dk \approx 2.3\times10^{33}\ {\rm erg\ cm^{-3}}, \qquad (3.6)$$

$$\epsilon_B = \int P_B(t,k)dk \approx 6.0\times10^{30}\ {\rm erg\ cm^{-3}}. \qquad (3.7)$$

These values correspond approximately to an averaged fluctuation velocity of $\delta v \approx 0.05c$ with typical density field of 10^{15} g/cm^3, and averaged magnetic-field strength of $\bar{B} \approx 10^{16}$ G. Even with the highest-resolution run, the equipartition is not achieved and this indicates that there is a room for further magnetic-field amplification.

IV. SATURATION OF THE MAGNETIC FIELD

Figure 8 plots the time evolution of the magnetic-field energy. The initial magnetic-field strength is 10^{13} G

for all the runs. The magnetic-field energy steeply increases for $t - t_{\rm mrg} \gtrsim 0$ ms and the amplification is more prominent in the higher-resolution runs. In the highest-resolution run with $\Delta x_{(l_{\rm max})} = 17.5$ m, the energy is amplified by a factor of $\approx 10^6$ at $t - t_{\rm mrg} \approx 4$ ms and this implies that the averaged magnetic-field strength increases up to $\sim 10^{16}$ G. The right hand-side panel of Fig. 8 plots the dependence of the growth rate of the magnetic-field energy on the finest grid resolution $\Delta x_{(l_{\rm max})}$. We fit the magnetic-field energy for 0 ms $\lesssim t - t_{\rm mrg} \lesssim 1$ ms by an exponentially growing function $\propto \exp(\sigma t)$. The figure shows a divergent feature of the growth rate with respect to $1/\Delta x_{(l_{\rm max})}$. Even with $\Delta x_{(l_{\rm max})} = 17.5$ m run, the saturation is not likely to be achieved. This behavior can be understood in terms of the property of the KH instability. As discussed in the previous subsection, the cut-off wavenumber $k_{\rm cutoff}$ of the KH instability increases with increasing the grid resolution. Therefore, the dispersion relation of the KH instability should be described as that of the shear layer with the infinitesimal thickness; $\sigma \propto k \propto 1/\Delta x_{(l_{\rm max})}$.

To explore the saturation energy of the magnetic field at the end of the kinematic amplification phase, we also perform simulations for an initial maximum magnetic-field strength varied from 10^{13} G to 10^{15} G. In Fig. 9, we plot E_B as a function of time. We overplot the results of the B13 run magnified by 10^2 and 10^4. Comparing the curve for the B14 run with $\Delta x_{(l_{\rm max})} = 17.5$ m to the magnified curve of the B13 run with the same resolution, we find a good overlap up to $t - t_{\rm mrg} \approx 2$ ms. This suggests that back reaction due to the amplified magnetic field is negligible. On the other hand for $t - t_{\rm mrg} \gtrsim 2$ ms, two curves do not overlap. This indicates that the back reaction probably due to magnetic braking turns on. At $t - t_{\rm mrg} \approx 5$ ms, the energy increases up to $\approx 10^{50}$ erg for the B14 run. For the B15 run with $\Delta x_{(l_{\rm max})} = 17.5$ m, the back reaction is turned on at $t - t_{\rm mrg} \approx 1$ ms and subsequently the energy reaches $\approx 4 \times 10^{50}$ erg at $t - t_{\rm mrg} \approx 3$ ms. The energy does not increase significantly after that. To assess the numerical effect on the saturation energy, we repeat the simulation with $\Delta x_{(l_{\rm max})} = 37.5$ m for the B15 run. Figure 9 shows that the energy is amplified only up to $\approx 5 \times 10^{49}$ erg at $t - t_{\rm mrg} \approx 5$ ms. Therefore, the saturation energy of the magnetic-field is likely to be $\gtrsim 4 \times 10^{50}$ erg and the averaged magnetic-field strength could be $\gtrsim 10^{16}$ G.

Figure 10 plots a spacetime diagram of the averaged angular velocity on the orbital plane

$$\bar{\Omega}(t, R) = \frac{1}{2\pi} \int_0^{2\pi} \Omega(t, R, z = 0, \varphi) d\varphi, \qquad (4.1)$$

where we employ cylindrical coordinates and Ω is an azimuthal component of the three velocity (v^φ). Because of the non-axisymetric structure of the HMNS, the angular momentum is transported outward. Figure 10 shows that the fluid elements moves gradually in the radial direction. The magnetic braking should be active in the Alfvén timescale

$$t_A = \frac{R_{\rm HMNS}}{v_A} \approx 2 \times 10^{-2} {\rm s} \left(\frac{\rho}{10^{15} {\rm g/cm^3}} \right)^{-1/2} \times \left(\frac{R_{\rm HMNS}}{20 {\rm km}} \right) \left(\frac{B}{10^{16} {\rm G}} \right)^{-1}, \qquad (4.2)$$

where $R_{\rm HMNS}$ and v_A are the HMNS radius and the Alfvén velocity, respectively. Although clear difference does not appear between the B13 and B15 runs in Fig. 10, we find that the magnetic braking works efficiently in the late phase of the HMNS evolution.

V. SUMMARY

We have performed high-resolution GRMHD simulations of the BNS mergers. Focusing on the shear layer emerging at the merger, the simulations were performed by assigning a finer grid resolution than the resolution in the previous simulations. With this resolution, we have revealed that the small-scale turbulence-like motion is developed due to the KH instability and the magnetic field is amplified efficiently. Starting from initial maximum magnetic-field strength of 10^{13} G, we have found that the magnetic-field energy is amplified at least by a factor of $\approx 10^6$ at ≈ 4 ms after the onset of the merger. Saturation energy of the magnetic-field is likely to be $\gtrsim 4 \times 10^{50}$ erg, which is $\gtrsim 0.1\%$ of the bulk kinetic energy. We should explore whether the physical saturation of the magnetic-field energy occurs below the equipartition value as a future work.

Our result shows that the efficient magnetic-field amplification during the BNS merger is realized in reality as pointed out in Refs. [12, 13]. This implies that it is always necessary to take into account the effects of high magnetic fields for modeling the post merger evolution of BNS.

ACKNOWLEDGMENTS

K. Kiuchi thanks to Andreas Bauswein and Sebastiano Bernuzzi for a discussion in University of Washington. Numerical computations were performed on K computer at AICS, XC30 at CfCA of NAOJ, FX10 at Information Technology Center of the University of Tokyo, and SR16000 at YITP of Kyoto University. This work was supported by Grant-in-Aid for Scientific Research (24244028, 15H00783,15H00836,15K05077,15H06857), for Scientific Research on Innovative Area (24103001), by HPCI Strategic Program of Japanese MEXT/JSPS (Project numbers hpci130025, 140211, and 150225), by the RIKEN iTHES Research Project, by the European Research Council (grant CAMAP-259276) and by local Spanish funds (grants AYA2013-40979-P and PROMETEOII/2014-069).

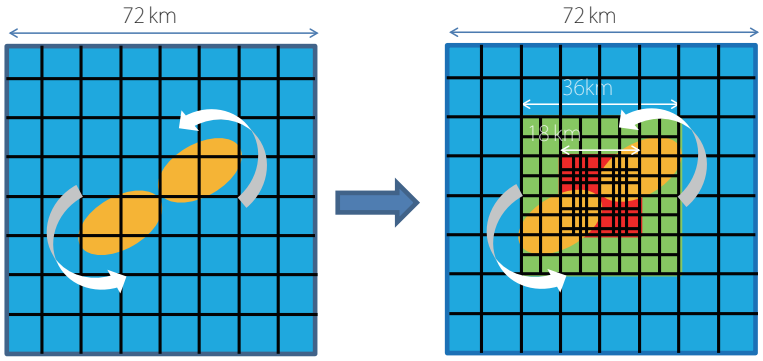

FIG. 1. Schematic picture of the refinement domains on the orbital plane for the initial grid configuration with $l = l^0_{\rm max}$ (left) and for the final grid configuration with $l = l_{\rm max} - 2(= l^0_{\rm max}), l_{\rm max} - 1$, and $l_{\rm max}$ (right). Two ellipses in the vicinity of the domain center represent the BNS just before the merger.

Appendix: Landau quantization effect

Because the magnetic-field strength exceeds the QED limit of 4.414×10^{13} G, the so-called Landau quantization would become important. The threshold density is characterized by the critical density

$$\rho_B = 7.04 \times 10^{10} \left(\frac{Y_e}{0.1}\right)^{-1} \left(\frac{B}{10^{16}{\rm G}}\right)^{3/2} {\rm g/cm^3}, \quad \text{(A.1)}$$

where Y_e is the electron fraction per baryon [40]. Below ρ_B, the ground Landau level is populated and the Landau quantization effect becomes important. On the other hand, for $\rho_B \ll \rho$, many Landau levels are populated and the magnetic field is not quantized. As shown in Fig. 2, the strong magnetic field exceeding the QED limit appears only in the high-density region. Therefore, the Landau quantization effect is irrelevant for the dynamics in the HMNS phase. Note that the range in which $\rho < \rho_B$ and $B^2/8\pi < \rho c^2$ are simultaneously satisfied is relatively narrow when the magnetic field is strong.

In this BNS model, the HMNS will collapse to a black hole (BH) at $t - t_{\rm mrg} \approx 10$ ms [20]. A massive accretion torus is formed after the BH formation. The density of the accretion torus is in the range of 10^{10-11} g/cm^3. Because of the efficient amplification of the magnetic field in the HMNS phase, the accretion torus would be strongly magnetized at its birth and the typical magnetic-field strength would be 10^{15} G at about 25 ms after the BH formation [20]. The Landau quantization might play an important role in the accretion torus phase because the density becomes the same order of ρ_B. With the energy difference between two Landau levels $\Delta E_{\rm Landau}$, the magnetic temperature is defined by

$$T_B \equiv \frac{\Delta E_{\rm Landau}}{k_B} = \left(\sqrt{1 + \frac{2B}{B_{\rm QED}}} - 1\right) \frac{m_e c^2}{k_B}, \quad \text{(A.2)}$$

where k_B, $B_{\rm QED}$, and m_e are the Boltzmann constant, the QED limit of the magnetic-field strength, and the electron rest mass, respectively [40]. The second equality holds for the density below ρ_B. If the temperature exceeds the magnetic temperature, the Landau quantization effect is diminished. With $B = 10^{15}$ G, $T_B \approx 3$–4 MeV$(B/10^{15}{\rm G})^{1/2}$. Because the typical temperature inside the accretion torus is ~ 10 MeV [41], the Landau quantization effect is irrelevant for the early accretion torus phase. However, in the neutrino cooling timescale, the temperature will decrease and this effect would become important.

[1] J. Abadie *et al.* Nucl. Instrum. Meth. A **624**, 223 (2010).
[2] T. Accadia *et al.* Class. Quant. Grav. **28**, 025005 (2011) [Erratum-ibid. **28**, 079501 (2011)].
[3] K. Kuroda, Class. Quant. Grav. **27**, 084004 (2010).
[4] R. Narayan, B. Paczynski and T. Piran, Astrophys. J. **395**, L83 (1992).
[5] J. M. Lattimer, & D. N. Schramm, Astrophys. J. **192**, L145 (1974).
[6] S. Wanajo, Y. Sekiguchi, N. Nishimura, K. Kiuchi, K. Kyutoku and M. Shibata, Astrophys. J. **789**, L39 (2014).
[7] Y. Sekiguchi, K. Kiuchi, K. Kyutoku and M. Shibata, Phys. Rev. D **91**, 064059 (2015).
[8] L. -X. Li and B. Paczynski, Astrophys. J. **507**, L59 (1998).
[9] N. R. Tanvir, A. J. Levan, A. S. Fruchter, J. Hjorth, R. A. Hounsell, K. Wiersema, & R. L. Tunnicliffe, Nature, **500**, 547 (2013).
[10] E. Berger, W. Fong, & R. Chornock, Astrophys. J. **774**, L23 (2013).
[11] D. R. Lorimer, Living Rev. Rel. **11**, 8 (2008).
[12] F. A. Rasio and S. L. Sapiro, Class. Quant. Grav. **16** R1-R29 (1999).
[13] D. Price and S. Rosswog, Science, **312**, 719 (2006).

[14] Y. T. Liu, S. L. Shapiro, Z. B. Etienne and K. Taniguchi, Phys. Rev. D **78**, 024012 (2008).

[15] M. Anderson, E. W. Hirschmann, L. Lehner, S. L. Liebling, P. M. Motl, D. Neilsen, C. Palenzuela and J. E. Tohline, Phys. Rev. Lett. **100**, 191101 (2008) .

[16] B. Giacomazzo, L. Rezzolla and L. Baiotti, Phys. Rev. D **83**, 044014 (2011).

[17] B. Giacomazzo, J. Zrake, P. Duffell, A. I. MacFadyen and R. Perna, Astrophys. J. **809**, no. 1, 39 (2015)

[18] K. Dionysopoulou, D. Alic and L. Rezzolla, Phys. Rev. D **92**, no. 8, 084064 (2015)

[19] C. Palenzuela, S. L. Liebling, D. Neilsen, L. Lehner, O. L. Caballero, E. OConnor and M. Anderson, Phys. Rev. D **92**, no. 4, 044045 (2015)

[20] K. Kiuchi, K. Kyutoku, Y. Sekiguchi, M. Shibata, T. Wada, Phys. Rev. D **90**, 041502(R), (2014).

[21] M. Obergaulinger, M. A. Aloy and E. Muller, Astron. Astrophys. **515**, A30 (2010)

[22] J. Zrake and A. I. MacFadyen, Astrophys. J. **769**, L29 (2013)

[23] K. Kiuchi, K. Kyutoku and M. Shibata, Phys. Rev. D **86**, 064008 (2012).

[24] M. Shibata and T. Nakamura, Phys. Rev. D **52**, 5428, (1995).

[25] T. W. Baumgarte and S. L. Shapiro, Phys. Rev. D **59**, 024007 (1998).

[26] M. Campanelli, C. O. Lousto, P. Marronetti, and Y. Zlochower, Phys. Rev. Lett. **96**, 111101 (2006).

[27] J. G. Baker, J. Centrella, D.-I. Choi, M. Koppitz, and J. van Meter, Phys. Rev. Lett. **96**, 111102 (2006).

[28] A. Kurganov and E. Tadmor, J. Comput. Phys. **160**, 241 (2000).

[29] D. Balsara. J.Comput.Phys.,**174**, 614 (2001).

[30] M. Bocquet, S. Bonazzola, E. Gourgoulhon, and J. Novak, Astron. Astrophys. **301**, 757 (1995).

[31] K. Kiuchi and K. Kotake, Mon. Not. Roy. Astron. Soc. **385**, 1327 (2008)

[32] A. Colaiuda, V. Ferrari, L. Gualtieri, and J. A. Pons, Mon. Not. R. Astron. Soc. **385**, 2080 (2007).

[33] N. K. Glendenning and S. A. Moszkowski, Phys. Rev. Lett. **67**, 2414 (1991).

[34] J. S. Read, B. D. Lackey, B. J. Owen, and J. L. Friedman, Phys. Rev. D **79**, 124032 (2009).

[35] K. Kiuchi, http://www2.yukawa.kyoto-u.ac.jp/˜kenta.kiuchi/GWRC/

[36] S. Chandrasekhar, Hydrodynamic and hydromagnetic stability, International Series of Monographs on Physics (Oxford: Clarendon) (1961)

[37] A. Miura, and P. L. Pritchett, J. Geophys. Res., **87**, 7431 (1982)

[38] R. Keppens, G. Toóth, R. H. J. Westermann, et al., J. Plasma Phys., **61**, 1 (1999)

[39] D. Ryu, T. W.Jones, and A. Frank, Astrophys. J., **545**, 475 (2000)

[40] A. K. Harding and D. Lai, Rept. Prog. Phys. **69**, 2631 (2006)

[41] We evaluate the temperature from the thermal component of the specific internal energy assuming the gas, photons, and relativistic electron positrons contribute the specific internal energy. The data of the specific internal energy is taken from Ref. [20].

[42] G. Falkovich, Phys. Fluids **6**, 1411 (1994)

[43] D.H. Porter, P.R. Woodward and A. Pouquet, Phys. Fluids **10**, 237 (1998)

[44] T. Gotoh, Comp. Phys. Comm. **147**, 530 (2002)

[45] Y. Kaneda, T. Ishihara, M. Yokokawa, K. Itakura, and A. Uno, Phys. Fluids **15**, L21 (2003)

[46] A. Brandenburg, Astrophys. J. 550, **824** (2001)

[47] A. Brandenburg and K. Subramanianb, Phys. Rep. **417**, 1 (2005)

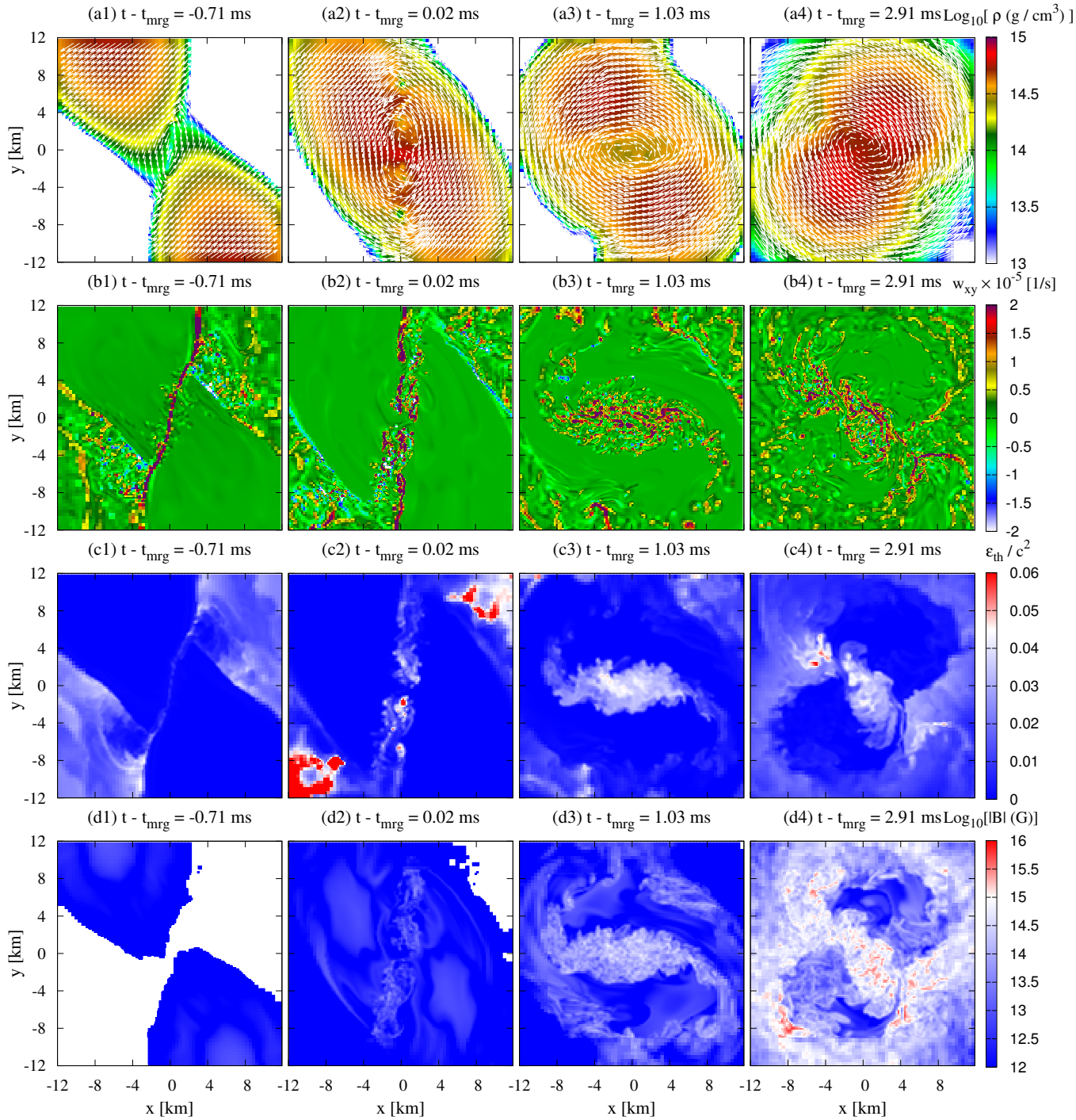
(a1) t - t_mrg = -0.71 ms
(a2) t - t_mrg = 0.02 ms
(a3) t - t_mrg = 1.03 ms
(a4) t - t_mrg = 2.91 ms
Log10[ρ (g / cm^3)]
(b1) t - t_mrg = -0.71 ms
(b2) t - t_mrg = 0.02 ms
(b3) t - t_mrg = 1.03 ms
(b4) t - t_mrg = 2.91 ms
w_xy × 10^-5 [1/s]
(c1) t - t_mrg = -0.71 ms
(c2) t - t_mrg = 0.02 ms
(c3) t - t_mrg = 1.03 ms
(c4) t - t_mrg = 2.91 ms
ε_th / c^2
(d1) t - t_mrg = -0.71 ms
(d2) t - t_mrg = 0.02 ms
(d3) t - t_mrg = 1.03 ms
(d4) t - t_mrg = 2.91 ms
Log10[|B| (G)]
y [km]
x [km]

FIG. 2. Profiles of the rest-mass density with velocity field (the 1st row), of the vorticity (the 2nd row), of the thermal component of the specific internal energy (the 3rd row), and of the magnetic-field strength (the 4th row) on the orbital plane. The initial magnetic-field strength is 10^{13} G and the resolution is $\Delta x_{(l_{\rm max})} = 17.5$ m. $t_{\rm mrg}$ is the merger time (see the text for details).

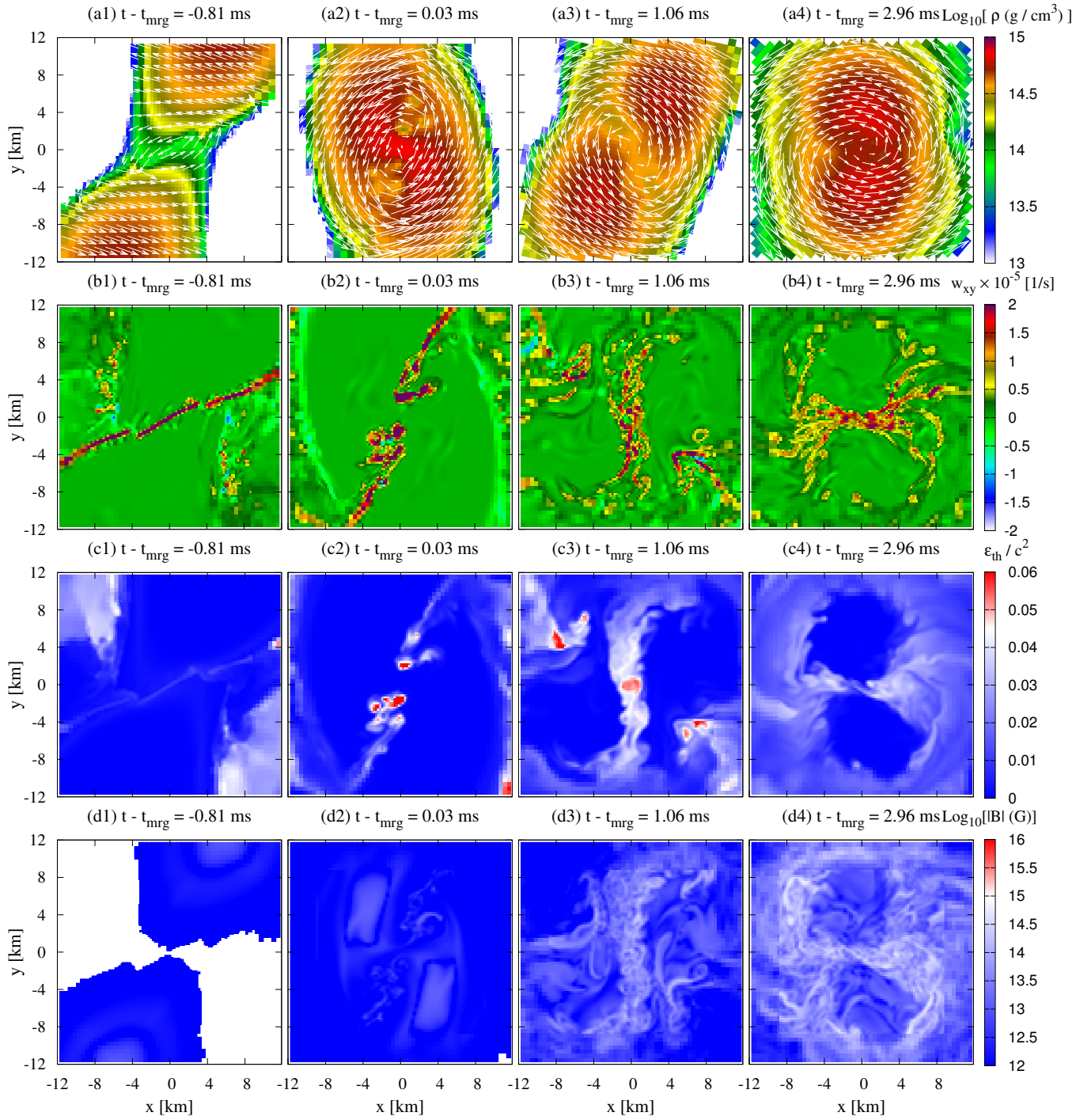
(a1) t - t_mrg = -0.81 ms
(a2) t - t_mrg = 0.03 ms
(a3) t - t_mrg = 1.06 ms
(a4) t - t_mrg = 2.96 ms
Log10[ρ (g / cm^3)]
(b1) t - t_mrg = -0.81 ms
(b2) t - t_mrg = 0.03 ms
(b3) t - t_mrg = 1.06 ms
(b4) t - t_mrg = 2.96 ms
w_xy × 10^-5 [1/s]
(c1) t - t_mrg = -0.81 ms
(c2) t - t_mrg = 0.03 ms
(c3) t - t_mrg = 1.06 ms
(c4) t - t_mrg = 2.96 ms
ε_th / c^2
(d1) t - t_mrg = -0.81 ms
(d2) t - t_mrg = 0.03 ms
(d3) t - t_mrg = 1.06 ms
(d4) t - t_mrg = 2.96 ms
Log10[|B| (G)]
y [km]
x [km]

FIG. 3. Same as Fig. 2, but for $\Delta x_{(l_{\max})} = 37.5$ m.

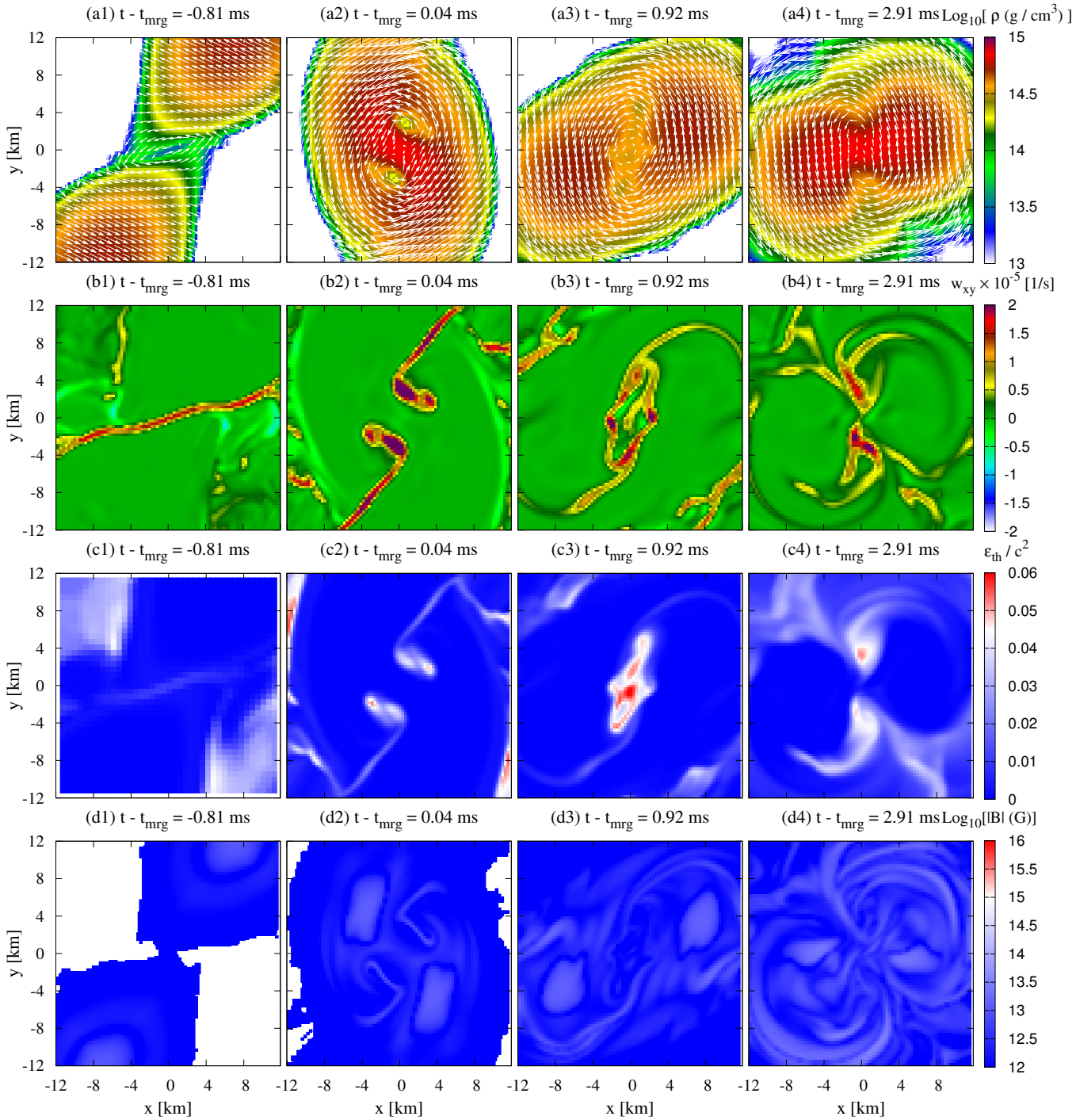
(a1) t - t_mrg = -0.81 ms
(a2) t - t_mrg = 0.04 ms
(a3) t - t_mrg = 0.92 ms
(a4) t - t_mrg = 2.91 ms
Log10[ρ (g / cm^3)]
(b1) t - t_mrg = -0.81 ms
(b2) t - t_mrg = 0.04 ms
(b3) t - t_mrg = 0.92 ms
(b4) t - t_mrg = 2.91 ms
w_xy × 10^-5 [1/s]
(c1) t - t_mrg = -0.81 ms
(c2) t - t_mrg = 0.04 ms
(c3) t - t_mrg = 0.92 ms
(c4) t - t_mrg = 2.91 ms
ε_th / c^2
(d1) t - t_mrg = -0.81 ms
(d2) t - t_mrg = 0.04 ms
(d3) t - t_mrg = 0.92 ms
(d4) t - t_mrg = 2.91 ms
Log10[|B| (G)]
y [km]
x [km]

FIG. 4. Same as Fig. 2, but for $\Delta x_{(l_{\max})} = 150$ m.

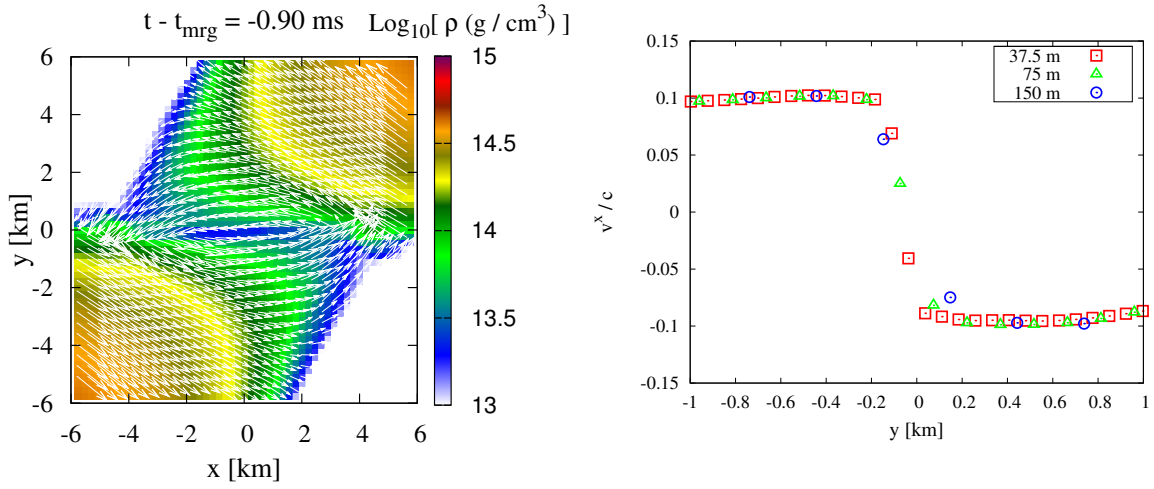

FIG. 5. (Left) Profile of the rest-mass density with velocity field on the orbital plane just before the onset of the merger and (right) profile of v^x in the left panel along the y axis with $x = 0$ km for $\Delta x_{(l_{\rm max})} = 37.5$, 75, and 150 m runs.

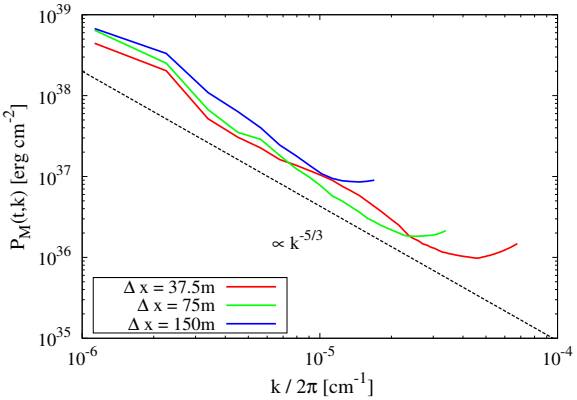

FIG. 6. Kinetic energy spectrum of the matter flow for $\Delta x_{(l_{\rm max})} = 37.5$, 75, and 150 m. The spectrum is evaluated at $t - t_{\rm mrg} = 2.0$ ms.

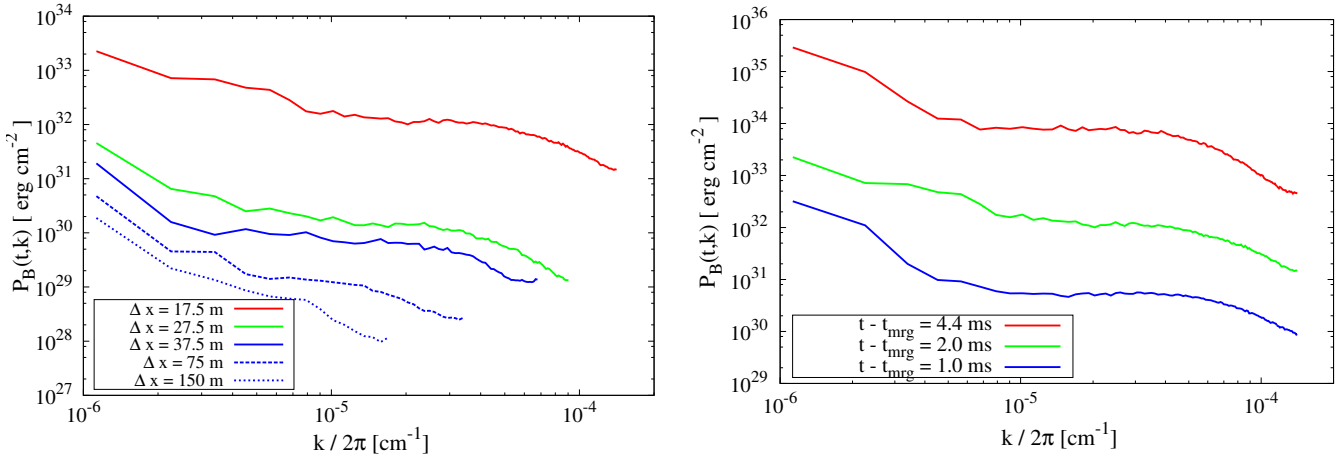

FIG. 7. Energy spectrum of the magnetic field for $\Delta x_{(l_{\max})} = 17.5$, 27.5, 37.5, 75, and 150 m runs at $t - t_{\rm mrg} = 2.0$ ms (left) and for $\Delta x_{(l_{\max})} = 17.5$ m run at $t - t_{\rm mrg} = 1.0, 2.0$, and 4.4 ms.

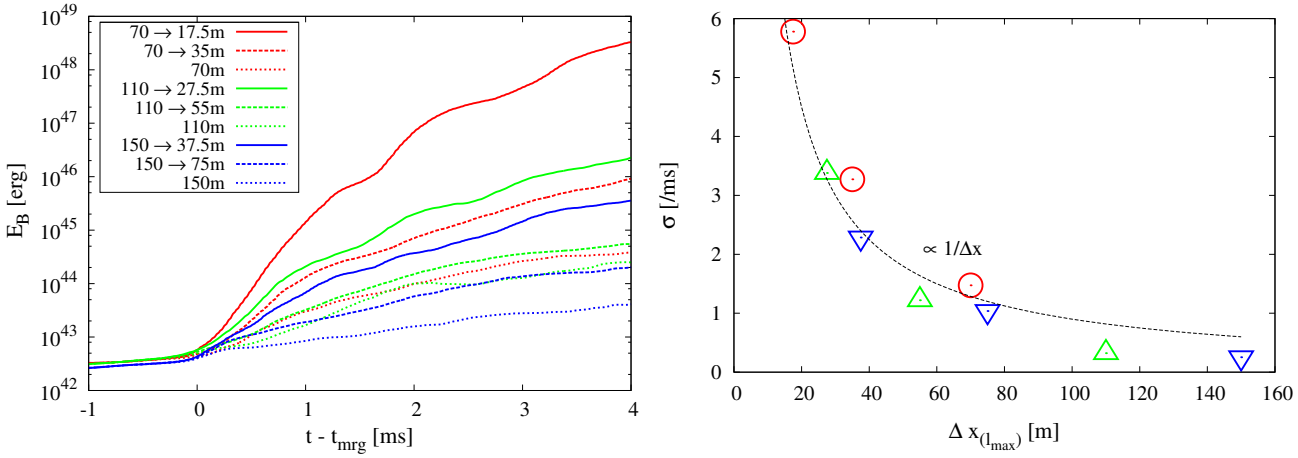

FIG. 8. (Left) Magnetic-field energy as a function of the time for the B13 run. (Right) The growth rate of the magnetic-field energy as a function of the final grid resolution.

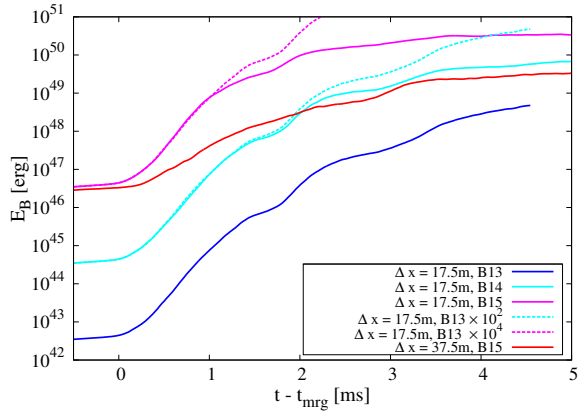

FIG. 9. Time evolution of the magnetic-field energy for the B13, B14, and B15 runs. The cyan- and magenta-dashed curves show the evolution of the B13 run magnified by 10^2 and 10^4, respectively.

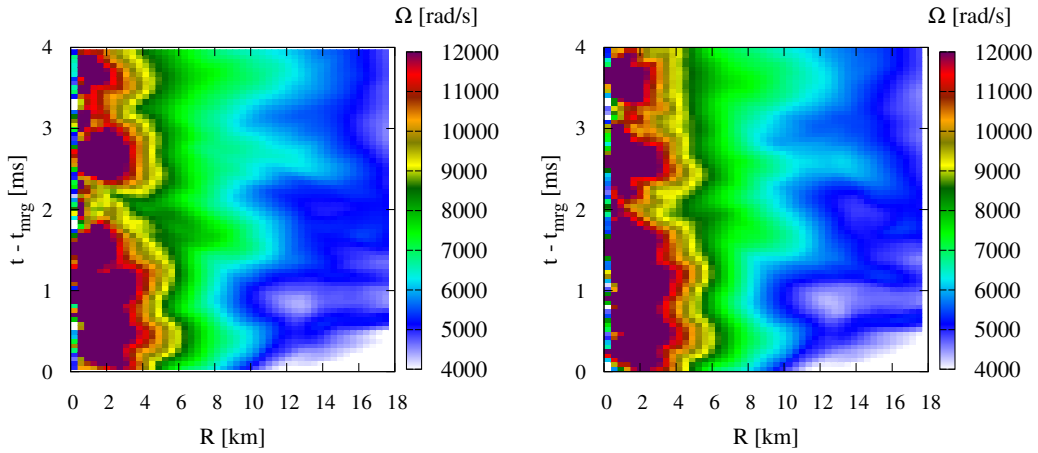

FIG. 10. Spacetime diagram of the angular velocity for the B13 run with $\Delta x_{(l_{\rm max})} = 17.5$ m (left) and the B15 run with $\Delta x_{(l_{\rm max})} = 17.5$ m (right). The horizontal axis is the radial coordinate and the angular velocity on the orbital plane is averaged in the azimuthal direction.